Princeton Plasma Physics Laboratory

PPPL- 5063

PPPL-5063

The Dependence of the Strength and Thickness of Field-Aligned Currents on Solar Wind and Ionospheric Parameters

Jay R. Johnson and Simon Wing

AUGUST 2014

PRINCETON PLASMA PHYSICS LABORATORY

Prepared for the U.S. Department of Energy under Contract DE-AC02-09CH11466.

The Dependence of the Strength and Thickness of Field-Aligned Currents on Solar Wind and Ionospheric Parameters

Jay R. Johnson[1] and Simon Wing[2]

[1]Princeton University, Plasma Physics Laboratory, Princeton, New Jersey, USA.

[2]Johns Hopkins University, Applied Physics Laboratory, Laurel, MD, USA.

Abstract. Sheared plasma flows at the low-latitude boundary layer correlate well with early afternoon auroral arcs and field-aligned currents [*Sonnerup*, 1980; *Lundin and Evans*, 1985]. We present a simple analytic model that relates solar wind and ionospheric parameters to the strength and thickness of field-aligned currents in a region of sheared velocity, such as the low-latitude boundary layer. We compare the predictions of the model with DMSP observations and find remarkably good scaling of the currents with solar wind and ionospheric parameters. The sheared boundary layer thickness is inferred to be around 3000km consistent with observational studies. The analytic model provides a simple way to organize data and to infer boundary layer structures from ionospheric data.

1. Introduction

The low-latitude boundary layer is a narrow region of persistent or intermittent flow located on the inner edge of the magnetopause [*Hones et al.*, 1972]. The boundary layer can play an important role in the transfer of mass, momentum, and energy from the solar wind to the magnetosphere [*Eastman et al.*, 1976]. One of the key features of the boundary layer is the transition in the plasma flow from magnetosheath flow velocity to the relatively stagnant flow in the magnetosphere. The velocity shear layer corresponds to a potential difference across the boundary, which can drive field-aligned currents [*Sonnerup*, 1980] into and out of the ionosphere as described by *Iijima and Potemra* [1976]. Moreover, plasma structures in the LLBL are well correlated with the occurrence of discrete auroral arcs at high latitude in the early afternoon. *Echim et al.* [2007, 2008] recently developed a 1D kinetic model that describes magnetosphere-ionosphere coupling in a sheared boundary layer and provides profiles of field-aligned currents, potential drop, and precipitating electron energy flux.

Recently, *Wing et al.* [2011], using DMSP particle (SSJ4) and magnetometer data, examined the dependence of solar wind driving of a few magnetosphere-ionosphere (M-I) coupling parameters, namely the maximum field-aligned current density ($J_{\|}$), peak electron energy (as a proxy for ($\Delta\phi_{\|}$), electron energy flux (ϵ) on solar wind velocity (V_{sw}) and solar wind density (n_{sw}). The model of [*Echim et al.*, 2008] captured the general dependencies of the dayside field-aligned currents on solar wind velocity and density, and suggests that much of the dependence of M-I coupling parameters could be understood in terms of such a model. Motivated by this work, we derive simple analytic expressions that capture the dependence of the field-aligned current and its spatial scale on solar wind and ionospheric parameters. We verify the analytical results through comparison with the rigorous approach of [*Echim et al.*, 2008], and we validate the model using the dataset used in the original study [*Wing et al.*, 2011]. The analytic solutions presented here provide a good framework for organizing the data and examining parameter scans.

2. The Field-Aligned Current for a Sheared Velocity Profile

The model of [*Echim et al.*, 2008] utilizes a kinetic approach for the magnetopause to compute a self-consistent boundary layer using prescribed density, temperature, and velocity moments in the magnetosheath and magnetosphere [*Echim et al.*, 2005]. The boundary layer model is coupled to the ionosphere through field-aligned currents, and solutions for the ionospheric potential are obtained by solving the current continuity equation in the ionosphere where the field-aligned currents are obtained from a nonlinear Knight relation [*Knight*, 1973].

In order to gain some simple understanding of the results presented in [*Echim et al.*, 2008], we consider the current continuity equation of the ionosphere

$$\nabla \cdot \Sigma_P \nabla \phi_i = j_{\|}(\phi_m, \phi_i) \tag{1}$$

where ϕ_m and ϕ_i are the potential in the magnetosphere and ionosphere respectively. As in [*Echim et al.*, 2008], the profile of ϕ_m is determined primarily by the solar wind magnetosphere interaction at the magnetopause. In our model, the potential drop between the magnetosphere and ionosphere drives a parallel current out of the ionosphere determined by a linear Knight relation [*Knight*, 1973]

$$j_{\|} = \kappa(\phi_i - \phi_m), \tag{2}$$

where $\kappa = n_e e^2/\sqrt{2\pi m_e T_e}$. The linear Knight relation is obtained from an expansion of the nonlinear current-voltage relation when $1 \ll e(\phi_i - \phi_m)/T_e \ll B_m/B_i$, where B_m and B_i are the magnetic field strength at the top and bottom of the potential drop. For simplicity, we will assume that κ is constant throughout the shear layer, recognizing that the current profiles will be controlled by the value of density and temperature close to the current maximum. Observationally the velocity shear layer tends to occur Earthward of the magnetopause density gradient [*Paschmann et al.*, 1993; *Phan and Paschmann*, 1996], so the relevant density may be that of the low-latitude boundary layer. Although the model of [*Echim et al.*, 2008] employed a nonlinear Knight relation with densities specified by a Vlasov equilibrium model, we find that the general characteristics of the analytic solutions that we obtain are similar to the numerical results presented in [*Echim et al.*, 2008].

Assuming constant conductivity and combining Equations 1 and 2, we find

$$\frac{\Sigma_P}{\kappa}\nabla^2\phi_i = (\phi_i - \phi_m) \tag{3}$$

As in *Lyons* [1980] and *Echim et al.* [2008] we solve this equation in one dimension with ϕ_m specified as a function of the spatial coordinate. Equation 3 can be solved for the ionospheric potential, ϕ_i using the method of Fourier transform where we take the Fourier transform of ϕ to be

$$\hat{\phi}(q) = \frac{1}{2\pi}\int_{-\infty}^{\infty} \phi(x)e^{-iqx}dx, \tag{4}$$

with the inverse transform

$$\phi(x) = \int_{-\infty}^{\infty} \hat{\phi}(q)e^{iqx}dq. \tag{5}$$

The Fourier transform of Equation 3 is

$$\hat{\phi}_i(q) = \left(\frac{1}{1+q^2L^2}\right)\hat{\phi}_m(q), \tag{6}$$

where $L = \sqrt{\Sigma_P/\kappa}$ is the well known electrostatic auroral scale length [*Lyons*, 1980]. From Equation 6 it is obvious that the ionospheric potential maps to the magnetospheric potential on scales larger than L (i.e. $qL \ll 1$) while a parallel potential drop can develop on smaller scales. The potential drop and field-aligned current are obtained in a similar manner by inverting their Fourier transforms,

$$\Delta\hat{\phi}(q) = \hat{\phi}_i(q) - \hat{\phi}_m(q) = -\left(\frac{q^2L^2}{1+q^2L^2}\right)\hat{\phi}_m(q) \tag{7}$$

$$\hat{j}_\parallel(q) = -\kappa\left(\frac{q^2L^2}{1+q^2L^2}\right)\hat{\phi}_m(q). \tag{8}$$

In the remainder of this paper we shall obtain and analyze the solution of Equation 8 to determine how the field-aligned current depends on the magnetopause profile (controlled by solar wind-magnetosphere interactions) and ionospheric conditions (controlled by solar radiation and particle precipitation).

While the model of *Echim et al.* [2007] specified the magnetospheric potential, ϕ_m, as the solution of a kinetic boundary layer model [*Echim et al.*, 2005], the general characteristics of the variation of the magnetospheric potential may also be specified by a more generic velocity (electric field) profile that retains the basic characteristics of the magnetopause boundary layer, which can be constrained by observations. The velocity profile in the boundary layer typically varies from an asymptotic flow, V_0, to little or no flow on the inner edge of the boundary layer over the thickness of the boundary layer, Δ_m. A simple velocity profile that captures these characteristics is

$$V_y(x_m) = \frac{V_0}{2}(1 + \tanh(x_m/\Delta_m)) \tag{9}$$

where x_m is the magnetospheric coordinate across the magnetopause boundary layer. This velocity profile is consistent with an electric field

$$E_x = -\frac{d\phi_m}{dx_m} = -V_y B_0 \tag{10}$$

which is supported by a potential of the following form

$$\phi_m(x_m) = \frac{V_0 B_0}{2}[x_m + \Delta_m \log(2\cosh(x_m/\Delta_m))] \tag{11}$$

where we have added an arbitrary constant so that the potential is zero at the inner (magnetospheric) edge of the LLBL.

To solve for the ionospheric potential in the ionosphere, it is necessary to express the magnetospheric potential as a function of the ionospheric coordinate at the ionospheric altitude, z_i. Using the simple conical mapping function used by *Echim et al.* [2007] and illustrated in Figure 1, we have $x_m = x_i\sqrt{B_i/B_m} \equiv x_i\sqrt{b}$, and at 200km, $\sqrt{b} = 32$. In this case

$$\phi_m(x_i) = \frac{V_0 B_0 \sqrt{b}}{2}\left[x_i + \Delta_i \log\left(2\cosh\left(x_i/\Delta_i\right)\right)\right] \tag{12}$$

where $\Delta_i \equiv \Delta_m/\sqrt{b}$ is the ionospheric scale length obtained by mapping the magnetospheric scale length to ionospheric altitude.

To proceed, we obtain the Fourier transform of ϕ_m derived in Appendix A.

$$\hat{\phi}_m(q) = \frac{1}{2\pi}\int \phi_m(x_i)e^{-iqx_i}dx_i = \frac{V_0 B_0\sqrt{b}}{2}\left[i\delta'(q) - \frac{\Delta_i}{2q\sinh(\pi\Delta_i q/2)}\right] \tag{13}$$

The current is then obtained from the inverse transform of Equation 8.

$$\begin{aligned} j_\parallel(x_i) &= -\kappa\int_{-\infty}^{\infty}\left(\frac{q^2L^2}{1+q^2L^2}\right)\hat{\phi}_m(q)e^{iqx_i}dq \\ &= \kappa\frac{V_0 B_0 \Delta_m}{2}\int_0^{\infty}\left(\frac{qL^2}{1+q^2L^2}\right)\frac{\cos(qx_i)}{\sinh(\pi\Delta_i q/2)}dq \end{aligned} \tag{14}$$

This integral may be solved without approximation using contour integration as shown in Appendix B.

$$j_{\|}(x_i) = \kappa \frac{V_0 B_0 \Delta_m}{2} \left[\frac{\pi}{2} \frac{e^{-|x_i|/L}}{\sin(\pi\alpha)} + \sum_{n=1}^{\infty} (-1)^n \frac{n e^{-2n|x_i|/\Delta_i}}{n^2 - \alpha^2} \right] \tag{15}$$

where $\alpha \equiv \Delta_i/2L$. The parallel current from Equation 15 is displayed in Figure 2 as a function of $|x_i|/L$ and α.

In this model, currents are driven by the potential difference across the boundary layer. If the potential maps to the ionosphere, the potential difference across the ionosphere drives a Pedersen current in the negative x direction. Because the electric field in the boundary layer vanishes asymptotically as $x \to -\infty$, the ionospheric current must be diverted upward in the shear layer to maintain current continuity. The current peaks at the center of the shear layer, and the current envelope is mostly controlled by the larger of the parameters L or Δ_i. In the case that the ionosphere is an insulator ($L \to 0$) it does not carry a current so there is no parallel current. When the ionosphere is a conductor, the current returns in a channel near the shear layer boundary. As the conductivity becomes larger ($L \to \infty$), the parallel current spreads over a larger and larger region. Similarly, if there is resistance ($\kappa \to 0$) along the field lines the parallel current must spread across field lines so that the total current can be returned. Detailed properties of the solution, such as the current maximum and width, will be further analyzed in the following sections.

3. Maximum Current

The current has an extremum at $x_i = 0$ as shown in Appendix C with a vanishing first derivative and negative second derivative (except the singular case, $\Delta_i \to 0$). The maximum value of the current is obtained by evaluating $j_{\parallel}(0)$

$$j_{\parallel,\mathrm{max}} = \kappa \frac{V_0 B_0 \Delta_m}{2} \left[\frac{\pi}{2\sin(\pi\alpha)} + \sum_{n=1}^{\infty} (-1)^n \frac{n}{n^2 - \alpha^2} \right], \tag{16}$$

which can be expressed (see Appendix C) in terms of the digamma function $\digamma(z) = d\log\Gamma(z)/dz$,

$$j_{\parallel,\mathrm{max}} = \kappa \frac{V_0 B_0 \Delta_m}{2} \left[\frac{1}{2\alpha} - \log 2 + \digamma(1+\alpha) - \digamma(1+\alpha/2) \right]. \tag{17}$$

This expression lends itself readily to numerical analysis because the digamma function is built into computational software programs such as Matlab and Mathematica.

It is instructive to examine the behavior of the maximum current in the limit of small and large α. In the limit that $\alpha \to 0$,

$$\digamma(1+\alpha) - \digamma(1+\alpha/2) = \mathcal{O}(\alpha) \tag{18}$$

so that

$$\lim_{\alpha\to 0} j_{\parallel,\mathrm{max}} \approx \kappa \frac{V_0 B_0 \Delta_m}{4\alpha} = \kappa \frac{V_0 B_0 L\sqrt{b}}{2} = \frac{1}{2} V_0 B_0 \sqrt{b\kappa\Sigma_P} \tag{19}$$

This result shows that the maximum current does not depend on the width of the shear layer when the shear layer maps to scales smaller than the auroral scale length, L.

For ($\alpha \gg 1$),

$$\digamma(1+\alpha) - \digamma(1+\alpha/2) = \log 2 - \frac{1}{2\alpha} + \frac{1}{4\alpha^2} - \frac{1}{8\alpha^4} + \mathcal{O}(\alpha^{-5}) \tag{20}$$

so that

$$\lim_{\alpha\to\infty} j_{\parallel,\mathrm{max}} \sim \kappa \frac{V_0 B_0 \Delta_m}{8\alpha^2} \sim \frac{\Sigma_P V_0 B_0 b}{2\Delta_m} \tag{21}$$

In the limit $\alpha \gg 1$ the magnetospheric potential maps to the ionosphere. Substituting

$\phi_i = \phi_m$ in Equation 1 and evaluating at $x_i = 0$ gives the same maximum current as in Equation 21.

It is also straightforward to construct a Padé approximation for the current that is uniformly valid for both small and large α. We may note that

$$[\frac{1}{2\alpha} - \log 2 + \digamma(1+\alpha) - \digamma(1+\alpha/2)] \sim \frac{1}{2\alpha(1+2\alpha)} \tag{22}$$

with a maximum relative error of 15% at $\alpha = 1$ and much less over most of the interval. Therefore, an excellent approximation for the maximum parallel current is

$$j_{\|,\mathrm{max}} \approx \kappa \frac{V_0 B_0 \Delta_m}{4\alpha(1+2\alpha)} = \frac{\Sigma_P V_0 B_0 b}{2(\Delta_m + \sqrt{b}L)} \tag{23}$$

With this simple relation, it is useful to consider how the current depends on solar wind and ionospheric parameters. The density profile in the sheath and boundary layer is roughly proportional to the solar wind density, so $L = \sqrt{\Sigma_P/\kappa} \sim n_{sw}^{-1/2}$. For conditions with $L \ll \Delta_i$ (high boundary layer density) the current is mostly controlled by the ionospheric conductance, solar wind velocity and boundary layer thickness. On the other hand, for low boundary layer density, $L \gg \Delta_i$, and $j_{\|,\mathrm{max}} \sim L^{-1} \sim \sqrt{n_{sw}}$, which is similar to the dependence seen in Figure 8 of *Echim et al.* [2008].

The maximum potential drop also corresponds to the maximum current at $x = 0$. In this case

$$\Delta\phi_{max} = \frac{j_\|}{\kappa} \approx \frac{V_0 B_0 \Delta_m}{4\alpha(1+2\alpha)} = \frac{V_0 B_0 \sqrt{b} L}{2} \frac{1}{(1 + \Delta_i/L)} \tag{24}$$

For $L \gg \Delta_i$, $\Delta\phi_{max} \sim L \sim n_{sw}^{-1/2}$, while for $L \ll \Delta_i$, $\Delta\phi_{max} \sim L^2 \sim n_{sw}^{-1}$. This behavior is consistent with the numerical solutions presented in *Echim et al.* [2008].

The dependence of the current and voltage on solar wind velocity is linear. This behavior is also similar to the solutions presented in Figure 6 of *Echim et al.* [2008].

The dependence of the current on the density, ionospheric conductivity, and shear layer width, Δ_m, is shown in Figure 3. From this figure, we see that parallel current increases with boundary layer density and conductivity, while it decreases with increased shear scale length.

4. Width of the Current Layer

The width of the current layer can be defined in a number of ways. We provide two alternative approaches to define the width based on the (a) curvature at the current maximum and (b) the full width at half maximum. The curvature provides insights as to the shape of the current near the current maximum, while the full width at half maximum provides more information about the global extent of the current profile.

Performing a Taylor expansion about the maximum current at $x = 0$, we find

$$j_{\|}(x) \approx j_{\|,\max}\left(1 - \frac{x_i^2}{2\sigma^2}\right) \tag{25}$$

where

$$\sigma \equiv \sqrt{\left.\frac{-j_{\|}}{d^2 j_{\|}/dx^2}\right|_{x=0}}. \tag{26}$$

Taking the second derivative of the current shown in Appendix D

$$\frac{d^2 j_{\|}}{dx^2} = \frac{j_{\|}}{L^2} - \kappa\frac{V_0 B_0 \Delta_m}{2}\frac{1}{\Delta_i^2 \cosh^2(x/\Delta_i)} \tag{27}$$

For $\alpha \ll 1$ we find that

$$\frac{1}{L^2} - \kappa\frac{V_0 B_0 \Delta_m}{2 j_{\|,max}\Delta_i^2} = \frac{1}{\Delta_i^2}\left[4\alpha^2 - \frac{1}{\frac{1}{2\alpha} - \log 2 + ...}\right] = \frac{-2\alpha}{\Delta_i^2}\left(1 + \mathcal{O}(\alpha)\right) \tag{28}$$

$$\sigma \approx \sqrt{\Delta L} \tag{29}$$

while for $\alpha \gg 1$

$$\frac{1}{L^2} - \kappa \frac{V_0 B_0 \Delta_m}{2 j_{\|,max} \Delta_i^2} \sim \frac{1}{\Delta_i^2} \left[4\alpha^2 - \frac{1}{\frac{1}{4\alpha^2} - \frac{1}{8\alpha^4} + ...} \right] \sim \frac{-2}{\Delta_i^2} \tag{30}$$

so that

$$\sigma \sim \frac{\Delta_i}{\sqrt{2}} \tag{31}$$

Then we can form a uniform approximation

$$\sigma = \sqrt{\Delta_i L (1 + \Delta_i / 2L)} \tag{32}$$

For a Gaussian distribution, with the same Taylor series, the width of the Gaussian would be σ and the full width at half maximum, Λ, would be

$$\Lambda = 2\sqrt{2 \ln 2} \sigma \approx 2.35 \sqrt{\Delta_i L (1 + \Delta_i / 2L)} \tag{33}$$

Alternatively, it is possible to determine the full width at half maximum directly from a numerical solution of Equation 15 as shown in Figure 2. The full width at half maximum can also be established analytically from the appropriate limits ($\alpha \to 0, \alpha \to \infty$) of $j_\|$.

In the limit of $\alpha \to 0$

$$\begin{aligned} j_\| &= \kappa \frac{V_0 B_0 \sqrt{b} L}{2} \left[e^{-|x_i|/L} + 2\alpha \sum_{n=1}^{\infty} (-1)^n \frac{(e^{-2|x_i|/\Delta_i})^n}{n} + O(\alpha^3) \right] \\ &= \kappa \frac{V_0 B_0 \sqrt{b} L}{2} \left[e^{-|x_i|/L} - 2\alpha \log(1 + e^{-2|x_i|/\Delta_i}) + O(\alpha^3) \right]. \end{aligned} \tag{34}$$

This solution (with $\alpha = 0$) was obtained by *Lyons* [1980] for a discontinuous electric field (velocity) profile. Solving for Λ such that $j_\|(\Lambda) = j_{\|,\mathrm{max}}/2$ with $\alpha \ll 1$ we find

$$\Lambda \approx 2 \ln 2 L (1 + 2\alpha) = 2 \ln 2 (L + \Delta_i) \tag{35}$$

For $\alpha \gg 1$ and $|x| \gg L$ we find

$$\begin{aligned} j_{\parallel} &= \kappa \frac{V_0 B_0 \Delta_m}{2} \left[-\frac{1}{\alpha^2} \sum_{n=1}^{\infty} (-1)^n n (e^{-2|x_i|/\Delta_i})^n + O(\alpha^{-4}) \right] \\ &= \kappa \frac{V_0 B_0 \Delta_m}{2} \left[\frac{1}{4\alpha^2 \cosh^2(x_i/\Delta_i)} + O(\alpha^{-4}) \right] \end{aligned} \quad (36)$$

Using Equation 21 for the current maximum

$$j_{\parallel}(\Lambda/2) = \frac{\kappa V_0 B_0 \Delta_m}{8\alpha^2 \cosh^2(\Lambda/2\Delta_i)} = \frac{j_{\parallel,\max}}{2} = \frac{\kappa V_0 B_0 \Delta_m}{16\alpha^2} \quad (37)$$

Then for $\alpha \gg 1$ we find that

$$\Lambda = 2\Delta_i \mathrm{arcosh}(\sqrt{2}) = 2\Delta_i \ln(1+\sqrt{2}) \quad (38)$$

A Padé approximation valid at small and large α may be constructed considering

$$\Lambda = \frac{2\ln 2L}{1 + c\alpha} + 2\ln(1+\sqrt{2})\Delta_i \quad (39)$$

by choosing c such that the power series for small α is satisfied. In this case

$$\Lambda \approx 2\ln 2L + 2[\ln(1+\sqrt{2}) - c\ln 2]\Delta_i \approx 2\ln 2(L + \Delta_i) \quad (40)$$

so that

$$c = 2\left[\frac{\ln(1+\sqrt{2})}{\ln 2} - 1 \right] \approx 0.5431 \quad (41)$$

and the result is accurate to within 5% for all values of α.

An even better approximation can be obtained by constraining the parameter, c, such that $\Lambda(\alpha = 1) = 4.6$ as obtained numerically. In this case, $c = 0.29$ which provides accuracy of the approximate solution within 1% for any value of α, so that

$$\Lambda = \frac{2\ln 2L}{1 + 0.29\alpha} + 2\ln(1+\sqrt{2})\Delta_i \quad (42)$$

In an earlier plot of the numerical solution of the parallel current (Figure 2) we showed the value of $|x_i|$where $j_\parallel = j_{\parallel,\max}/2$. In Figure 4 we provide the numerical value of the full width half maximum and for comparison the approximation shown in Equation 42 as well as the percentage error between the curves. It should also be noted that the width of the velocity shear layer, Δ_i, can also be obtained from measurement of Λ and L by solving for the positive root of

$$1.0224\alpha^2 + (3.5255 - 0.29\Lambda/L)\alpha - (\Lambda/L - 1.3863) = 0 \tag{43}$$

for $\Lambda > 2\ln 2L$.

For comparison, in the limit of large α, the value of the full width half maximum assuming a Gaussian defined by σ from Equation 33 is $\Lambda = 2\sqrt{\ln 2}\Delta_i = 1.67\Delta_i$, which can be compared with $\Lambda = 2\ln(1+\sqrt{2})\Delta_i = 1.76\Delta_i$ from Equation 42. On the other hand, the Gaussian fit based on curvature does not provide a good estimate of Λ at small α. Close examination of Equation 34 shows that the solution in the limit $\Delta \to 0$ is proportional to $e^{-|x_i|/L}$, which is an exponential decay, so it is not surprising that a Gaussian expansion would not fit the current profile in this limit. It is also clear that for a discontinuous velocity profile the current always spreads over an exponential envelope with a width determined by the auroral scale length, L, as previously discussed by *Lyons* [1980]

It is apparent from our results that the current layer thickness has no dependence on solar wind velocity. This behavior is consistent with the numerical solutions shown in Figure 6 of [*Echim et al.*, 2008]. On the other hand, the current layer does depend on the density of the solar wind because $L \sim n_{sw}^{-1/2}$ so that for $\Delta_i \ll L$ the width, $\Lambda \sim n_{sw}^{-1/2}$, decreases with increasing density as shown in Figure 8 of *Echim et al.* [2008]. This behavior is consistent with the fact that $\Delta_i \ll L$ for the parameters used in *Echim et al.* [2008].

5. Data Analysis

We now utilize the theoretical model to organize and interpret satellite data obtained from regions of upward field-aligned current and to validate the model. *Wing et al.* [2010] and *Wing et al.* [2011] have examined dayside field-aligned currents and precipitating populations. They found that much of the region 1 (R1) currents on the dayside are associated with boundary layer plasma suggesting the importance of boundary layer processes in determining the currents. In this study, we restrict ourselves to regions of upward R1 currents where a simple Knight-like current-voltage relation would be appropriate. From satellite data, we are able to measure the currents and thickness (latitudinal width) of current layers as described below. The solar wind parameters are inferred from satellite observations. Some ionospheric parameters are inferred from satellite observations and some from empirical models. We compare the dependence of currents on the solar wind parameters with predictions of the analytic model. We are able to infer the structure of the velocity shear layer from low altitude observations.

6. Data Sources and Techniques

This study utilizes a subset of the DMSP dataset used in the *Wing et al.* [2010] and *Wing et al.* [2011] studies, which includes over 20 years (1983-2006) of simultaneous DMSP magnetic field and particle precipitation observations. Solar wind data are obtained from ACE, WIND, IMP8, ISEE1, and ISEE3 observations. As described in *Wing et al.* [2010] and *Wing et al.* [2011] the solar wind and IMF parameters are propagated to the nominal magnetopause boundary, where 30 minute averages are computed for each field-aligned current event.

Field-aligned currents events are identified using the *Higuchi and Ohtani* [2000] algorithm on DMSP data. The field-aligned current events are associated with field-aligned precipitation, which is used to identify the the particle source regions using an automated algorithm [*Newell and Meng*, 1988; *Newell et al.*, 1991a, b, c] that was developed to determine whether the origins of the precipitating particles in the magnetosphere or solar wind. An important piece of information that these particle signatures provide is whether the precipitation occurs on boundary layer, open or closed field lines. For this study we restrict the data to those obtained in upward R1 that are located at the boundary layer and open-field lines.

7. FAC Latitudinal Width (Λ)

The relationship between of the thickness of the boundary layer (Δ) and the FAC latitudinal width (Λ) has not been previously explored in depth, if at all. The theoretical development in Section 4 can provide a framework to do this. In particular, Equations 35 and 38 provide expressions for the latitudinal width of the field-aligned current (Λ) for $\alpha \ll 1$ and $\alpha \gg 1$, respectively, where $\alpha = \Delta_i/(2L)$, Δ_i = thickness of the boundary layer mapped to the ionosphere, $L = \sqrt{\Sigma_p/\kappa}$, Σ_p = Pedersen conductivity, and κ = Knight conductivity, and Equation 42 gives a general expression relating Λ to Δ_i and L.

First, we investigate how Λ in the upward R1 boundary layer/open field regions varies with n_{sw}. The upward current is carried mostly by precipitating electrons. We use simultaneous particle precipitation to select FAC that is located at the boundary layer and open-field lines as described in Section 6. Basically, we select only passes where R1 is entirely located in LLBL, cusp, mantle, or/and polar rain. Λ is obtained by applying the *Higuchi and Ohtani* [2000] algorithm to DMSP magnetometer data as described in Section 6. For comparison with the theoretical model, we note that the density dependence in the model comes through κ, which corresponds to the density of the electron source population that carries the field aligned currents, which can range between the sheath and magnetospheric density, but most likely corresponds to LLBL densities. Because the density in the boundary layer scales with the solar wind density in the kinetic boundary layer models [*Echim et al.*, 2008], the solar wind density (which is monitored continuously) can provide a reasonable proxy for the boundary layer density. For conditions satisfying $\alpha \ll 1$, Equation 35 suggests that $\Lambda \sim L \sim {n_{sw}}^{-1/2}$.

Figure 5 shows log Λ vs. log n_{sw}, for $\Lambda/L < 5$ (small α) at 1100 - 1700 MLT. The selection of this range of Λ/L is based on Figure 4, which shows that $\alpha < 1$ corresponds to $\Lambda/L < 4.6$. The *Higuchi and Ohtani* [2000] algorithm only detects large scale FACs and has a minimum threshold of Λ of about 30 km. There are 97 points that satisfy the criteria. Figure 5 shows that the all the points tend to lie along the lines of slope = -0.5, suggesting that $\Lambda \sim n_{sw}^{-0.5}$, which is consistent with Equation 35. The least square fit yields $\log(\Lambda) = (0.47 \pm 0.06)\log(n_{sw}) + (5.1 \pm 0.05)$ or $\Lambda \sim {n_{sw}}^{-(0.47\pm0.06)}$. The correlation is highly significant, with $r = -0.60$ and probability for two uncorrelated variables to give $|r| = 0.60$ is < 0.01 ($P < 0.01$). We note that the anti-correlation of Λ with n_{sw} is also consistent with the model calculation of *Echim et al.* [2008].

Next, we examine how Λ varies with L. $L = \sqrt{\Sigma_p/\kappa}$ is calculated using empirical formulas for Σ_p and solar wind parameters to infer κ. $\Sigma_p = \Sigma_p(\text{solarillumination}) + \Sigma_p(\text{electronprecipitation})$ where $\Sigma_p(\text{solarillumination}) = 0.88(S_a\cos\chi)^{1/2}$ *Robinson and*

Vondrak [1984] and $\Sigma_p(\text{electronprecipitation}) = (40\langle E_e\rangle\epsilon^{1/2})/(16+\langle E_e\rangle^2)$ *Robinson et al.* [1987] where $\langle E_e\rangle$ = mean electron energy in keV, ϵ = electron energy flux in ergs/cm^2, S_a = the 10.7 cm solar radio flux, χ = the solar zenith angle. $\kappa = n_e e^2/\sqrt{2\pi m_e T_e}$ is computed using $n_e = n_{sw}$ [e.g. *Scudder et al.*, 1973; *Phan and Paschmann*, 1996] and $T_e = 10^6$K [e.g. *Phan and Paschmann*, 1996]. As in Figure 5, we restrict the observations to 1100–1700 magnetic local time (MLT), although most of the points come from 1100–1300 MLT because the frequency of the upward R1 located on the boundary layer or open-field lines decreases in the late afternoon and near dusk [*Wing et al.*, 2010].

Figure 6 shows log Λ vs. log L for $\Lambda/L < 5$, as in Figure 5. Lines with a slope of 1 (note that $\Lambda \sim L$ for $\alpha \ll 1$ from Equation 35) are also shown in Figure 6. As can be seen in the figure, the lines fit the points fairly well. The figure and Equation 35 suggest that $J_\parallel$ becomes more localized as L decreases. The least square fit yields log(Λ) = (0.9 $\pm$0.1) log(L) + (0.9 $\pm$ 0.5) or $\Lambda \sim L^{(0.9\pm0.1)}$. The correlation is highly significant, r = 0.74 and $P < 0.01$. The large scatter likely results from uncertainties in the estimates of Σ_p and κ. The estimation of Σ_p relies on the accuracies of the *Robinson et al.* [1987] and *Robinson and Vondrak* [1984] empirical formulas and the accuracies of $\langle E_e\rangle$, ϵ, and solar EUV flux. The estimation of κ relies on the accuracies of estimations of our proxies for n_e and T_e. Section 10 discusses further the sources of uncertainty in this and other figures.

8. Thickness of the Boundary Layer (Δ)

From Equations 42 and 43, one can obtain Δ_i from L and Λ, both of which can be observed, as discussed in Section 7. By definition, $\Delta_m/\Delta_i \sim \sqrt{B_m/B_i}$ and assuming $B_m/B_i \sim 1000$, we can also obtain Δ_m. Moreover, Δ_m can also be obtained from Equation 23, which relates Δ_m to $J_\parallel$, Σ_p, L, V_0, and B_0, which can estimated using observations and empirical formulas. We use the solar wind velocity, V_{sw}, as a proxy for the velocity shear in the boundary layer. For simplicity, we use the approximation V_0 at the magnetopause $V_0 = 0.20V_{sw}$ and B_0=20 nT. This value is similar to observations of the velocity shear and magnetic field at the low latitude boundary layer between noon and the dusk flank [e.g. *Fujimoto et al.*, 1998; *Vaisberg et al.*, 2001]. These parameters can then be used to obtain Δ_m using Equation 23.

Figure 7a and 7b plot log Δ_m as a function of V_{sw} where Δ_m is obtained independently from Equations 42 and 23, respectively. Figure 7 shows that Δ_m obtained from either method has roughly the same value, but the scatter is slightly larger for Δ_m obtained from Equation 23 as might be expected because there are fewer parameters in Equation 42. The maximum and minimum of Δ_m in Figure 7a are 1.5×10^7 and 5.6×10^4 m, respectively, whereas the maximum and minimum of Δ_m in Figure 7b are 1.6×10^7 and 2.8×10^4 m, respectively. The first and third quartile values in Figure 7a are 1.1×10^6 and 4.4×10^6 m, respectively, whereas the corresponding values in Figure 7b are 9.4×10^5 and 4.3×10^6 m, respectively. The mean value of $\Delta_m \sim 3 \times 10^6$m ($\sim 0.5R_E$) using either Equation 42 or Equation 23. The boundary layer thickness obtained from the two methods are consistent with each other and with previously reported values of the boundary layer thickness, [e.g. *Eastman and Hones*, 1979; *Phan and Paschmann*, 1996; *Šafránková et al.*, 2007].

Figure 7 also shows that Δ_m, from either method, does not have strong dependence on V_{sw}. It might be expected that the KH mode would become more unstableas V_{sw} increases, which could lead to more magnetosheath plasma entry and a wider LLBL. However, most of the observed FACs come from 11– 13 MLT, which map to the dayside magnetopause where the magnetosheath velocity is small and the KH modes may not have adequate time to grow convectively. Moreover, *Matsumoto and Seki* [2010] performed an MHD simulation of the boundary layer and found that even in the nonlinear stage, Δ_m does not change much with V_{sw}. Hence, their simulation result is qualitatively consistent with the Δ_m derived from these observations. Because KHI is expected to develop more fully along the flanks, where the field-lines map to late afternoon-dusk or early morning-dawn sectors, it would be interesting to examine whether FACs along the flanks might correspond with KH structures.

Figure 7 shows that the scatter can be quite large. However, in situ observations at the boundary layer also reveal similar variability in boundary layer thickness [e.g. *Eastman and Hones*, 1979; *Phan and Paschmann*, 1996; *Šafránková et al.*, 2007]. Nonetheless, some of the scatter can be attributed to the uncertainties in the parameters used to calculate Δ_m. Section 10 discusses some of the sources of these uncertainties.

9. Field-Aligned Current Density ($J_\parallel$)

Next, we investigate how $J_\parallel$ varies with Δ_m and Σ_p. The dependence of $J_\parallel$ on the thickness of the boundary layer is shown in Figure 8, which plots log $J_\parallel$ vs. log Δ_m. $J_\parallel$ is obtained directly from DMSP magnetometer observations, while Δ_m is obtained from Equation 42 and measured values of Λ and L. Figure 8 shows that the points tend to line along lines with a slope of -1, which is expected from the large α limit of Equation 23. The least square fit of the points for $\Lambda/L > 5$ has a slope of -0.8 ± 0.2, which is within the theoretical prediction of Equation 23. On the other hand, for $\Lambda/L < 5$, in the small α limit, the slope for the green dots is larger than -1 and closer to 0 because Equation 19 shows that $J_\parallel$ becomes independent of Δ_m in that limit.

The dependence of $J_\parallel$ on Σ_p is shown in Figure 9, which plots log $J_\parallel$ vs. log Σ_p. Here, $J_\parallel$ is obtained from DMSP magnetometer observations while Σ_p is obtained from DMSP SSJ4 observations, F10.7 record, and *Robinson and Vondrak* [1984] and *Robinson et al.* [1987] empirical formulas. Because the data come from the 11 – 17 MLT, Σ_p is mainly attributed to solar extreme ultra violet (EUV) as proxied by F10.7. To the first order, $J_\parallel$ increases with Σ_p, as would be expected. Higher conductivity makes it easier for the currents to flow. However, the dependence of $J_\parallel$ on Σ_p has a dependence on Λ/L or α. For $\Lambda/L > 20$ ($\alpha \gg 1$), $J_\parallel \sim \Sigma_p$, as suggested by Equation 21, but for values of $\alpha \ll 1$, $J_\parallel \sim \sqrt{\Sigma_p}$, as suggested by Equation 19. Figure 9a plots log $J_\parallel$ vs. log Σ_p for $\Lambda/L < 5$. The points tend to lie along the lines with slope of 0.5, which is consistent with Equation 19. Figure 9b plots log $J_\parallel$ vs. log Σ_p for $\Lambda/L > 20$. The points tend to lie along the lines with slope of 1, which is consistent with Equation 21. The scatter in Figures 8 and 9 are quite large because of the large number of parameters and the large uncertainties in each dependency parameters as indicated in Equations 19 and 21. In particular, in Figure 9a, the fit of the data points to the contours with slope 0.5 is not as good as the fit of the contours with slope of 1 in Figure 9b. *Wang et al.* [2005] also found large scatter in their $J_\parallel$ vs. Σ_p plot, although they combined upward and downward currents for 11 - 13 MLT. Section 10 discusses the source of errors in our plot.

Figure 10 plots log $J_\parallel$ vs. log n_{sw} for small α ($\Lambda/L < 3$). $J_\parallel$ is obtained from DMSP magnetometer observations while n_{sw} is obtained from solar wind observations. Figure 10 also plots lines with slope = 0.5, which is the expected slope from Equations 23 or 19. The figure shows that the points tend to line up along these lines, although the scatter is large. The least square fit results in $J_\parallel \sim n_{sw}^{(0.3\pm0.2)}$.

Figure 11 plots log $J_{\parallel}$ vs. log V_{sw} for small for MLT = 13 – 17. The reason for selecting these locations is that near noon, FAC would map to near the subsolar magnetopause where the boundary layer V would be small, which would not fit easily with points that come from the afternoon region, which map to magnetopause flank. $J_{\parallel}$ is obtained from DMSP magnetometer observations while V_{sw} is obtained from solar wind observations. Figure 11 also plots lines with slope = 1, which is the expected slope from Equations 23. This figure shows that the points tend to line up along these lines, but the fit is not very good (the scatter is large). The least square fit results in $J_{\parallel} \sim V_{sw}^{(0.7\pm0.6)}$.

The large scatter in Figures 11 and 10 may result from the anti-correlation between V_{sw} and n_{sw} [e.g., *Richardson et al.*, 1996], e.g., the effect of large V_{sw} would tend to oppose the effect of small n_{sw} and vice versa. This and other source of errors are discussed in Section 10.

10. Sources of uncertainties

Figures 5– 9 show that the data scales relatively well with expected power law dependence from the analytical relationships. However, the data exhibits significant scatter. In this section we discuss possible sources of uncertainty that may contribute to this scatter. We select the FAC data covering 11–17 MLT, which maps to the magnetopause region ranging from the pre-noon all the way to the dusk flank or even the nightside flank. In our analysis we assume simple scaling relations between the solar wind parameters and those in the boundary layer, assuming V_0= 0.20 V_{sw} and magnetosheath $n = n_{sw}$, respectively. While a simple scaling relation may be adequate to capture power law dependence, parameters such as velocity and density obviously vary along the flanks and in the boundary layer leading to large scatter in the data. The realistic value of V_0 may vary by a factor of

2 or 3 [e.g., *Fujimoto et al.*, 1998; *Phan et al.*, 1997; *Vaisberg et al.*, 2001; *Dimmock and Nykyri*, 2013], but because the plots are in log-log format, this difference would amount to a shift in the Y-intercept by 0.3-0.5, which would translate to scatter by that amount for those parameters that depend on V_0. Similar considerations also apply to the magnetosheath density. Additionally, V_{sw} anti-correlates with n_{sw} [e.g., *Richardson et al.*, 1996], which complicates the efforts to isolate the effects of V_{sw} or n_{sw}. Σ_p is estimated from *Robinson and Vondrak* [1984] and *Robinson et al.* [1987] empirical formulas, both of which have uncertainties. The Knight κ parameter was calculated from n_e, which was obtained from solar wind observation, but T_e is assumed to be 1×10^6 K [*Phan et al.*, 1997]. We have also used $B_0 = 20$ nT [e.g., *Phan et al.*, 1997; *Vaisberg et al.*, 2001]. A variation by a factor of 2 would introduce a shift in the Y-direction by 0.3, as the case for V_0. Interestingly, many of our equations have the product $V_0 B_0$, e.g., Equation 23, but at the boundary layer, from the subsolar region to the dusk flank, V_0 would increase while B_0 would decrease. Hence, the product would not vary much, as can be seen in MHD simulations (S. Merkin, private communication). Thus, although the parameters that depend on V_{sw} have large scatter, as shown in Figure 11, the parameters that depend on the product $V_{sw} B_0$ may have less scatter. The value of $b = B_m/B_i$ is assumed to be 1000, but in reality, it can vary along the flank.

In addition to uncertainties in parameters, the model itself has limitations. In particular, the model assumes a linear current-voltage relationship, which ignores thermal current and nonlinear saturation as well as restricting the magentospheric electron distribution function to be Maxwellian. Observations of intense localized peaks in current associated with energetic electron flux generally suggests that the current exceeds the thermal current, $j_{th} = nev_{the}/\sqrt{2\pi}$. While most of the currents observed in this study exceed typical thermal currents in the boundary layer, the weaker currents may be comparable ($j_{th} \sim 0.1 - 1\mu\text{A/m}^2$ for $n \sim 0.5 - 10\text{cm}^{-3}$ and $T_e \sim 100\text{eV}$); however, scaling relations may still apply even when the currents are comparable. Moreover, most of the scaling relations shown in this paper are tested with a subset of data with $\alpha < 1$ ($\Lambda/L < 5$), which have currents that are generally much larger than the thermal current. Finally, because the dayside currents are relatively weak ($j_{\|} \ll j_{th}b$), nonlinear corrections are unnecessary.

Although the linear approximation may lead to an overestimate of field-aligned potential when thermal currents are significant, the remarkable similarity of the analytical scaling relations with observations and their similarity to the maximum current and width to the numerical solutions of *Echim et al.* [2008] suggest that the simple relations probably capture the most important physical dependencies on the solar wind and ionospheric parameters.

11. Summary and Conclusion

Our study provides a theoretical framework to analyze the coupling between the magnetosphere and ionosphere near the magnetopause boundary. We have developed simplified analytical expressions for the dependence of the currents and their structure on solar wind and ionospheric parameters that provide similar dependence as nonlinear kinetic models of the boundary layer. Using simultaneous measurements of solar wind and DMSP particle and magnetometer data, we examined how the M-I coupling parameters $J_{\|}$, Δ, Λ , Σ_p, and κ vary with each other and solar wind parameters and found that the observations are well organized by our simple analytical expressions. We examined how the mapping of boundary layer structure, Δ_m, maps to ionospheric scales, Λ, and how the mapping depends on the auroral electrostatic scale length, L. Our results indicate that using low altitude and solar wind observations, we can use the observed Λ at low altitude to infer Δ_m reasonably well and these methods could serve as the basis for development of general tools for inferring boundary layer structures [*Simon Wedlund et al.*, 2013].

Appendix A: Fourier Transform of ϕ_m

The Fourier transform of the magnetospheric potential

$$\phi_m(x) = \frac{V_0 B_0 \sqrt{b}}{2} \left[x + \Delta_i \log\left(2\cosh\left(x/\Delta_i\right)\right)\right] \tag{A1}$$

can be obtained as follows: The Fourier transform of x is

$$\frac{1}{2\pi}\int_{-\infty}^{\infty} x e^{-iqx} dx = i\frac{d}{dq}\left[\frac{1}{2\pi}\int_{-\infty}^{\infty} e^{-iqx} dx\right] = i\delta'(q) \tag{A2}$$

where $'$ is a derivative with respect to q and $\delta(q)$ is the Dirac delta function,

$$\delta(q) \equiv \frac{1}{2\pi}\int_{-\infty}^{\infty} e^{-iqx} dx. \tag{A3}$$

The Fourier transform of $\Delta_i \log(2\cosh(x/\Delta_i))$,

$$\hat{\phi}(q) = \frac{1}{2\pi}\int_{-\infty}^{\infty} \Delta_i \log(2\cosh(x/\Delta_i)) e^{-iqx} dx \tag{A4}$$

is obtained through integration in the complex plane. The integral may be evaluated by deforming the contour of integration along the negative real axis as shown in Figure 12. Branch points are located at

$$z_{b,n} = -i\frac{\pi\Delta_i}{2}(1+2n) \tag{A5}$$

where $n \in \mathbb{Z}$. It is to be noted that $\hat{\phi}(q)$ is an even function in q, so in our evaluation, we only need consider $q > 0$, in which case the integration can be performed analytically along the five paths, $\mathcal{C}_1, \cdots, \mathcal{C}_5$ shown in Figure 12. The integrals along the great arcs, $\mathcal{C}_1$ and $\mathcal{C}_5$, vanish as the radius of the arc approaches ∞. The contribution from the small segment, $\mathcal{C}_3$, with $-\epsilon < z < \epsilon$ also vanishes in the limit $\epsilon \to 0$

$$I_{\mathcal{C}_3}(\epsilon) = \frac{\Delta_i}{2\pi}\int_{-\epsilon}^{\epsilon} \log(2\cosh(z/\Delta_i))e^{-iqz}dz = \frac{\Delta_i}{\pi}\log(2)\epsilon + O(\epsilon^3);\ \lim_{\epsilon\to 0} I_{\mathcal{C}_3}(\epsilon) = 0. \quad \text{(A6)}$$

The only non vanishing contributions arise from the integration along $\mathcal{C}_2$ and $\mathcal{C}_4$. For convenience, this integration is performed along the path $z_{\pm} = -iy\pi\Delta/2 \pm \epsilon$, where z_- follows the path from $y = \infty$ to $y = 0$ and z_+ follows the path from $y = 0$ to $y = \infty$. We now consider the behavior of $\zeta(z) = 2\cosh(z/\Delta_i)$ along the paths $z_{\pm}$ in the limit of small ϵ

$$\begin{aligned}
\zeta_{\pm}(y) &= 2\cosh(\pm\epsilon - iy\pi/2) \\
&= 2\cosh(\epsilon)\cos(y\pi/2) \mp 2i\sinh(\epsilon)\sin(y\pi/2) \\
&\approx 2\cos(y\pi/2) \mp 2i\epsilon\sin(y\pi/2) \qquad \text{(A7)}
\end{aligned}$$

In the complex plane, this function ζ_+ (ζ_-) oscillates clockwise (counterclockwise) in an ellipse around the origin as y increases. The argument of $\zeta_{\pm}$ is obviously multivalued. At $y = 0$, $\zeta_{\pm}$ are on the same Principal branch defined with $-\pi < \mathrm{Arg}(z) \leq \pi$. In the limit that $\epsilon \to 0$, whenever a branch point, $y = 2n + 1$ for $n \in \mathbb{Z}$, is passed the argument of ζ_+ (ζ_-) decreases (increases) by π, and the difference in argument, $(\arg(\zeta_+) - \arg(\zeta_-))$, decreases by 2π. Consequently

$$\log(\zeta_+) - \log(\zeta_-) = -2\pi ni; \qquad 2n - 1 < y < 2n + 1 \qquad \text{(A8)}$$

because $|\zeta_+| = |\zeta_-|$.

Performing the integrations

$$\begin{aligned}
\hat{\phi}(q) &= \frac{1}{2\pi}\left(\int_{\mathcal{C}_2} \Delta_i \log(2\cosh(z/\Delta_i))e^{-iqz}dz - \int_{\mathcal{C}_4} \Delta_i \log(2\cosh(z/\Delta_i))e^{-iqz}dz\right) \\
&= \frac{i\Delta_i}{2\pi}\int_0^\infty \left(\arg(\zeta_+) - \arg(\zeta_-)\right) e^{-\pi q\Delta_i y/2}\left(\frac{-i\pi\Delta_i}{2}\right) dy + O(\epsilon) \\
&= \frac{\Delta_i^2}{4}\sum_{n=1}^\infty \int_{2n-1}^{2n+1} (-2\pi n) e^{-\pi q\Delta_i y/2} dy \\
&= \frac{\Delta_i}{q}\sum_{n=1}^\infty n\left[e^{-\pi q\Delta_i y/2}\right]_{2n-1}^{2n+1} \\
&= -\frac{\Delta_i}{q}\sum_{n=1}^\infty n e^{-\pi q\Delta_i n}(e^{\pi q\Delta_i/2} - e^{-\pi q\Delta_i/2}) = -\frac{2\Delta_i}{q}\sinh(\pi q\Delta_i/2)\sum_{n=0}^\infty n e^{-\pi q\Delta_i n} \\
&= -\frac{2\Delta_i}{q}\sinh(\pi q\Delta_i/2)\frac{e^{-\pi q\Delta_i}}{(1-e^{-\pi q\Delta_i})^2} = -\frac{\Delta_i}{2q\sinh(\pi q\Delta_i/2)} \qquad \text{(A9)}
\end{aligned}$$

Therefore the Fourier transform

$$\Delta_i \log(2\cosh(x/\Delta_i)) \mapsto_{\mathcal{F}} -\frac{\Delta_i}{2q\sinh(\pi q\Delta_i/2)}. \qquad \text{(A10)}$$

Combining this transform with Equation A2 we obtain Equation 13.

As a confirmation, consider

$$\phi_m(x_i) = \frac{V_0 B_0\sqrt{b}}{2}\int_{-\infty}^{\infty}\left(i\delta'(q) - \frac{\Delta_i}{2q\sinh(\pi\Delta_i q/2)}\right) e^{iqx_i} dq \qquad \text{(A11)}$$

Differentiating

$$\begin{aligned}
d\phi_m/dx_i &= \frac{V_0 B_0\sqrt{b}}{2}\int_{-\infty}^{\infty}\left(-q\delta'(q) - \frac{i\Delta_i}{2}\frac{1}{\sinh(\pi\Delta_i q/2)}\right) e^{iqx_i} dq \\
&= \frac{V_0 B_0\sqrt{b}}{2}\left(1 + \Delta_i\int_0^\infty \frac{\sin(qx_i)}{\sinh(\pi\Delta_i q/2)} dq\right) \\
&= \frac{V_0 B_0\sqrt{b}}{2}\left(1 + \tanh(x_i/\Delta_i)\right) \qquad \text{(A12)}
\end{aligned}$$

[using 4.111 from *Gradshteyn and Ryzhik*, 2007], which is consistent with the velocity profile (Equation 9).

Appendix B: Contour Integration of $j_\|$

The current is obtained from

$$j_\| = \frac{V_0 B_0 \Delta_m}{4} \int_{-\infty}^{\infty} \left(\frac{\Sigma_P q}{1 + \Sigma_P q^2/\kappa} \right) \frac{\cos(qx)}{\sinh(\pi \Delta_i q/2)} dq \tag{B1}$$

For $x > 0$ the contour may be closed in the upper half plane, in which case we encircle poles located at $q = i\sqrt{\kappa/\Sigma_P} = i/L$ and $q = 2in/\Delta$, for n=1,2,.... Note that there is no pole at $q = 0$ where the integrand is well behaved. Then

$$j_\| = \frac{V_0 B_0 \Delta_m}{4} \left(2\pi i \sum_j \mathrm{Res}(f, z_j) \right) \tag{B2}$$

where

$$z_0 = i/L; z_n = 2in/\Delta_i, n = 1, 2, ...; f(z) = \left(\frac{\Sigma_P q^2}{1 + \Sigma_P q^2/\kappa} \right) \left(\frac{e^{iqx}}{q \sinh(\pi \Delta_i q/2)} \right) \tag{B3}$$

For $n = 0$

$$\mathrm{Res}(f, z_0) = -i \frac{\kappa}{2} \frac{e^{-x/L}}{\sin(\pi \Delta_i/2L)} \tag{B4}$$

and for $n \geq 1$

$$\mathrm{Res}(f, z_n) = -i(-1)^n \left(\frac{\kappa}{n\pi} \right) \left(\frac{e^{-2nx/\Delta_i}}{1 - (\Delta_i/2nL)^2} \right) \tag{B5}$$

so that

$$j_\| = \kappa \frac{V_0 B_0 \Delta_m}{2} \left[\frac{\pi}{2} \frac{e^{-x/L}}{\sin(\pi\Delta/2L)} + \sum_{n=1}^{\infty} (-1)^n \frac{n e^{-2nx/\Delta}}{n^2 - (\Delta/2L)^2} \right] \tag{B6}$$

Following the same procedure for $x < 0$ and closing the path in the lower complex plane leads to Equation 15 valid for all x.

Appendix C: The Location and Value of Maximum Current

The location of the current maximum occurs at the extremum. Because $j_\parallel$ is an even function of x it is expected that an extremum is found at $x = 0$. To verify, we compute

$$\begin{aligned}
\frac{dj_\parallel}{dx} &= -\kappa\frac{V_0 B_0 \Delta_m \mathrm{sgn}(x)}{2}\left[\frac{\pi}{2L}\frac{e^{-|x|/L}}{\sin(\pi\alpha)} + \frac{2}{\Delta_i}\sum_{n=1}^{\infty}(-1)^n\frac{n^2}{n^2-\alpha^2}e^{-2n|x|/\Delta_i}\right] \\
&= -\kappa\frac{V_0 B_0 \Delta_m \mathrm{sgn}(x)}{2}\left[\frac{\pi}{2L}\frac{e^{-|x|/L}}{\sin(\pi\alpha)} + \frac{2\alpha^2}{\Delta_i}\sum_{n=1}^{\infty}(-1)^n\frac{e^{-2n|x|/\Delta_i}}{n^2-\alpha^2} + \frac{2}{\Delta_i}\sum_{n=1}^{\infty}(-1)^n e^{-2n|x|/\Delta_i}\right] \\
&= -\kappa\frac{V_0 B_0 \Delta_m \mathrm{sgn}(x)}{2}\left[\frac{\pi}{2L}\frac{e^{-|x|/L}}{\sin(\pi\alpha)} + \frac{2\alpha^2}{\Delta_i}\sum_{n=1}^{\infty}(-1)^n\frac{e^{-2n|x|/\Delta_i}}{n^2-\alpha^2} - \frac{e^{-|x|/\Delta_i}}{\Delta_i\cosh(x/\Delta_i)}\right]
\end{aligned}$$

where $\alpha \equiv \Delta_i/2L$, and we have used

$$\sum_{n=1}^{\infty}x^n = \sum_{n=0}^{\infty}x^n - 1 = \frac{1}{1-x} - 1 = -\frac{x}{1-x} \tag{C1}$$

to simplify

$$\sum_{n=1}^{\infty}\left(-e^{-2|x|/\Delta_i}\right)^n = -\frac{e^{-|x|/\Delta_i}}{2\cosh(x/\Delta_i)} \tag{C2}$$

Taking the limit as $x \to 0$

$$\lim_{x\to 0}\frac{dj_\parallel}{dx} = -\kappa\frac{V_0 B_0 \Delta_m \mathrm{sgn}(x)}{2}\left[\frac{\pi}{2L}\frac{1}{\sin(\pi\alpha)} + \frac{2\alpha^2}{\Delta_i}\sum_{n=1}^{\infty}\frac{(-1)^n}{n^2-\alpha^2} - \frac{1}{\Delta_i}\right] \tag{C3}$$

The infinite sum is simplified as follows

$$\sum_{n=1}^{\infty}\frac{(-1)^n}{n^2-\alpha^2} = -\frac{1}{2\alpha}\sum_{n=1}^{\infty}(-1)^n\left(\frac{1}{n+\alpha} - \frac{1}{n-\alpha}\right) \tag{C4}$$

and

$$\sum_{n=1}^{\infty}\frac{(-1)^n}{n+\alpha} = \frac{1}{2}\left[\sum_{m=1}^{\infty}\frac{1}{m+\alpha/2} - \sum_{m=1}^{\infty}\frac{1}{m+(\alpha-1)/2}\right] = \frac{1}{2}\left[\digamma(1/2+\alpha/2) - \digamma(1+\alpha/2)\right] \tag{C5}$$

where $\digamma(z) = d\log\Gamma(z)/dz$ is the digamma function. Then

$$\begin{aligned}\sum_{n=1}^{\infty}\frac{(-1)^n}{n^2-\alpha^2} &= -\frac{1}{4\alpha}\left[\digamma(1/2+\alpha/2)-\digamma(1/2-\alpha/2)+\digamma(1-\alpha/2)-\digamma(1+\alpha/2)\right] \\ &= -\frac{\pi}{2\alpha}\frac{1}{\sin(\pi\alpha)}+\frac{1}{2\alpha^2}\end{aligned}$$

Where we have utilized the recurrance and reflection formulae for the digamma function (A&S 6.3.7) to simplify the expression

$$\begin{aligned}\digamma(1+z) &= \digamma(z)+1/z \\ \digamma(1-z) &= \digamma(z)+\pi\cot\pi z \\ \digamma(1/2-z) &= \digamma(1/2+z)-\pi\tan\pi z\end{aligned}$$

so that

$$\left[\frac{\pi}{2L}\frac{1}{\sin(\pi\alpha)}+\frac{2\alpha^2}{\Delta_i}\sum_{n=1}^{\infty}\frac{(-1)^n}{n^2-\alpha^2}-\frac{1}{\Delta_i}\right]\rightarrow\left[\frac{\pi}{2L}\frac{1}{\sin(\pi\alpha)}+\frac{2\alpha^2}{\Delta_i}\left(-\frac{\pi}{2\alpha}\frac{1}{\sin(\pi\alpha)}+\frac{1}{2\alpha^2}\right)-\frac{1}{\Delta_i}\right]\rightarrow 0 \tag{C6}$$

and the first derivative of the current vanishes at $x=0$. That this extremum is a maximum in the current is shown when we compute the curvature to obtain the current width.

The current evaluated at $x=0$ is

$$j_{\parallel,\max}=\kappa\frac{V_0B_0\Delta_m}{2}\left[\frac{\pi}{2}\frac{1}{\sin(\pi\Delta_i/2L)}+\sum_{n=1}^{\infty}(-1)^n\frac{n}{n^2-(\Delta_i/2L)^2}\right], \tag{C7}$$

The summation may be computed as follows

$$\begin{aligned}\sum_{n=1}^{\infty}(-1)^n\frac{n}{n^2-\alpha^2} &= \frac{1}{2}\sum_{n=1}^{\infty}(-1)^n\left[\frac{1}{n+\alpha}+\frac{1}{n-\alpha}\right] \\ &= \frac{1}{4}\left[\digamma(1/2+\alpha/2)+\digamma(1/2-\alpha/2)-\digamma(1+\alpha/2)-\digamma(1-\alpha/2)\right]\end{aligned}$$

Using the reflection and recurrence formulae as well as the duplication forumula

$$\digamma(1/2+z)=2\digamma(2z)-\digamma(z)-2\log 2 \tag{C8}$$

we find that

$$\begin{aligned}
\sum_{n=1}^{\infty}(-1)^n \frac{n}{n^2-\alpha^2} &= -\frac{\pi}{2}\frac{1}{\sin(\pi\alpha)} - \frac{1}{4}\left[\digamma(1+\alpha/2) - 2\digamma(1/2+\alpha/2) + \digamma(\alpha/2)\right] \\
&= \frac{1}{2\alpha}\left(1 - \frac{\pi\alpha}{\sin(\pi\alpha)}\right) + \digamma(1+\alpha) - \digamma(1+\alpha/2) - \log 2
\end{aligned}$$

so that

$$j_{\parallel,\max} = \kappa\frac{V_0 B_0 \Delta_m}{2}\left[\frac{1}{2\alpha} - \log 2 + \digamma(1+\alpha) - \digamma(1+\alpha/2)\right] \quad \text{(C9)}$$

Appendix D: The Current Width

The current width, Λ, defined in Equation 26 is obtained from the analytic solution for $j_\parallel$ given in Equation 15

$$\begin{aligned}
\frac{d^2 j_\parallel}{dx^2} &= \kappa\frac{V_0 B_0 \Delta_m}{2}\left[\frac{\pi}{2L^2}\frac{e^{-|x|/L}}{\sin(\pi\Delta_i/2L)} + \frac{4}{\Delta_i^2}\sum_{n=1}^{\infty}(-1)^n\frac{n^3 e^{-2n|x|/\Delta_i}}{n^2-(\Delta_i/2L)^2}\right] \\
&= \kappa\frac{V_0 B_0 \Delta_m}{2L^2}\left[\frac{\pi}{2}\frac{e^{-|x|/L}}{\sin(\pi\alpha)} + \sum_{n=1}^{\infty}(-1)^n\frac{n e^{-2n|x|/\Delta_i}}{n^2-\alpha^2} + \alpha^{-2}\sum_{n=1}^{\infty}(-1)^n n e^{-2n|x|/\Delta_i}\right] \\
&= \frac{j_\parallel}{L^2} - \kappa\frac{V_0 B_0 \Delta_m}{2}\frac{1}{\Delta_i^2\cosh^2(x/\Delta_i)}
\end{aligned}$$

where we have used the following

$$\sum_1^{\infty} n x^n = x\frac{d}{dx}\sum_0^{\infty} x^n = \frac{x}{(1-x)^2} \quad \text{(D1)}$$

so that

$$\sum_1^{\infty} n\left(-e^{-2|x|/L}\right)^n = -\frac{1}{4\cosh^2(x/\Delta_i)} \quad \text{(D2)}$$

Acknowledgments.

Simon Wing acknowledges supports from NSF Grants AGS-1058456 and ATM-0802715; and NASA Grant NNX13XAE12G. Jay R. Johnson acknowledges support from NASA grants (NNH09AM53I, NNH09AK63I, NNH11AR07I), NSF grant ATM0902730, AGS-1203299 and DOE contract DE-AC02-09CH11466. We thank Fred Rich, Gordon Wilson, and the Air Force Research Laboratory for the DMSP SSJ4 and magnetometer data. We thank James M. Weygand for the solar wind data processing. The raw solar wind data from ACE, Wind, IMP8, ISEE1 and ISEE3 were obtained from NASA CDAW and NSSDC.

References

Dimmock, A. P., and K. Nykyri (2013), The statistical mapping of magnetosheath plasma properties based on THEMIS measurements in the magnetosheath interplanetary medium reference frame, *Journal of Geophysical Research (Space Physics)*, *118*, 4963–4976, doi:10.1002/jgra.50465.

Eastman, T. E., and E. W. Hones, Jr. (1979), Characteristics of the magnetospheric boundary layer and magnetopause layer as observed by Imp 6, *J. Geophys. Res.*, *84*, 2019–2028, doi:10.1029/JA084iA05p02019.

Eastman, T. E., E. W. Hones, Jr., S. J. Bame, and J. R. Asbridge (1976), The magnetospheric boundary layer - Site of plasma, momentum and energy transfer from the magnetosheath into the magnetosphere, *Geophys. Res. Lett.*, *3*, 685–688, doi:10.1029/GL003i011p00685.

Echim, M. M., J. F. Lemaire, and M. Roth (2005), Self-consistent solution for a collisionless plasma slab in motion across a magnetic field, *Phys. Plasmas*, *12*(7), 072,904, doi:10.1063/1.1943848.

Echim, M. M., M. Roth, and J. de Keyser (2007), Sheared magnetospheric plasma flows and discrete auroral arcs: a quasi-static coupling model, *Annales Geophysicae*, *25*, 317–330, doi:10.5194/angeo-25-317-2007.

Echim, M. M., M. Roth, and J. de Keyser (2008), Ionospheric feedback effects on the quasi-stationary coupling between LLBL and postnoon/evening discrete auroral arcs, *Annales Geophysicae*, *26*, 913–928, doi:10.5194/angeo-26-913-2008.

Fujimoto, M., T. Mukai, H. Kawano, M. Nakamura, A. Nishida, Y. Saito, T. Yamamoto, and S. Kokubun (1998), Structure of the low-latitude boundary layer: A case study with Geotail data, *J. Geophys. Res.,* , *103*, 2297–2308, doi:10.1029/97JA02946.

Gradshteyn, I. S., and I. M. Ryzhik (2007), *Table of integrals, series, and products*, seventh ed., xlviii+1171 pp., Elsevier/Academic Press, Amsterdam, translated from the Russian, Translation edited and with a preface by Alan Jeffrey and Daniel Zwillinger, With one CD-ROM (Windows, Macintosh and UNIX).

Higuchi, T., and S.-i. Ohtani (2000), Automatic identification of large-scale field-aligned current structures, *J. Geophys. Res.*, *105*, 25,305–25,316, doi:10.1029/2000JA900073.

Hones, E. W., J. R. Asbridge, S. J. Bame, M. D. Montgomery, S. Singer, and S.-I. Akasofu (1972), Measurements of magnetotail plasma flow made with vela 4b, *J. Geophys. Res.*, *77*(28), 5503–5522, doi:10.1029/JA077i028p05503.

Iijima, T., and T. A. Potemra (1976), The amplitude distribution of field-aligned currents at northern high latitudes observed by Triad, *J. Geophys. Res.*, *81*, 2165–2174, doi:10.1029/JA081i013p02165.

Knight, S. (1973), Parallel electric fields, *Planet*, *21*, 741–750.

Lundin, R., and D. S. Evans (1985), Boundary layer plasmas as a source for high-latitude, early afternoon, auroral arcs, *Planet. Space Sci.*, *33*, 1389–1406, doi:10.1016/0032-0633(85)90115-1.

Lyons, L. R. (1980), Generation of large-scale regions of auroral currents, electric potentials, and precipitation by the divergence of the convection electric field, *J. Geophys. Res.*, *85*, 17–24, doi:10.1029/JA085iA01p00017.

Matsumoto, Y., and K. Seki (2010), Formation of a broad plasma turbulent layer by forward and inverse energy cascades of the Kelvin-Helmholtz instability, *J. Geophys. Res.*, *115*, A10231, doi:10.1029/2009JA014637.

Newell, P. T., and C.-I. Meng (1988), The cusp and the cleft/boundary layer - Low-altitude identification and statistical local time variation, *J. Geophys. Res.*, *931*, 14,549–14,556, doi:10.1029/JA093iA12p14549.

Newell, P. T., C.-I. Meng, E. R. Sanchez, W. J. Burke, and M. E. Greenspan (1991a), Identification and observations of the plasma mantle at low altitude, *J. Geophys. Res.*, *96*, 35–45, doi:10.1029/90JA01760.

Newell, P. T., S. Wing, C.-I. Meng, and V. Sigillito (1991b), The auroral oval position, structure, and intensity of precipitation from 1984 onward - An automated on-line data base, *J. Geophys. Res.*, *96*, 5877–5882, doi:10.1029/90JA02450.

Newell, P. T., E. R. Sanchez, C.-I. Meng, W. J. Burke, M. E. Greenspan, and C. R. Clauer (1991c), The low-latitude boundary layer and the boundary plasma sheet at low altitude - Prenoon precipitation regions and convection reversal boundaries, *J. Geophys. Res.*, *962*, 21,013, doi:10.1029/91JA01818.

Paschmann, G., W. Baumjohann, N. Sckopke, T.-D. Phan, and H. Luehr (1993), Structure of the dayside magnetopause for low magnetic shear, *J. Geophys. Res.*, *981*, 13,409, doi: 10.1029/93JA00646.

Phan, T. D., and G. Paschmann (1996), Low-latitude dayside magnetopause and boundary layer for high magnetic shear 1. Structure and motion, *J. Geophys. Res.*, *101*, 7801–7816, doi:10.1029/95JA03752.

Phan, T. D., D. Larson, J. McFadden, R. P. Lin, C. Carlson, M. Moyer, K. I. Paularena, M. McCarthy, G. K. Parks, H. Rème, T. R. Sanderson, and R. P. Lepping (1997), Low-latitude dusk flank magnetosheath, magnetopause, and boundary layer for low magnetic shear: Wind observations, *J. Geophys. Res.,* , *102*, 19,883–19,896, doi: 10.1029/97JA01596.

Richardson, J. D., J. W. Belcher, A. J. Lazarus, K. I. Paularena, and P. R. Gazis (1996), Statistical properties of the solar wind, in *American Institute of Physics Conference Series*, *American Institute of Physics Conference Series*, vol. 382, edited by D. Winterhalter, J. T. Gosling, S. R. Habbal, W. S. Kurth, and M. Neugebauer, pp. 483–486, doi:10.1063/1.51433.

Robinson, R. M., and R. R. Vondrak (1984), Measurements of E region ionization and conductivity produced by solar illumination at high latitudes, *J. Geophys. Res.*, *89*, 3951–3956, doi:10.1029/JA089iA06p03951.

Robinson, R. M., R. R. Vondrak, K. Miller, T. Dabbs, and D. Hardy (1987), On calculating ionospheric conductances from the flux and energy of precipitating electrons, *J. Geophys. Res.*, *92*, 2565–2569, doi:10.1029/JA092iA03p02565.

Šafránková, J., Z. Němeček, L. Přech, J. Šimůnek, D. Sibeck, and J.-A. Sauvaud (2007), Variations of the flank llbl thickness as response to the solar wind dynamic pressure and imf orientation, *Journal of Geophysical Research: Space Physics*, *112*(A7), n/a–n/a, doi:10.1029/2006JA011889.

Scudder, J. D., D. L. Lind, and K. W. Ogilvie (1973), Electron observations in the solar wind and magnetosheath., *J. Geophys. Res.*, *78*, 6535–6548, doi:10.1029/JA078i028p06535.

Simon Wedlund, C., H. Lamy, B. Gustavsson, T. Sergienko, and U. Brändström (2013), Estimating energy spectra of electron precipitation above auroral arcs from ground-based observations with radar and optics, *Journal of Geophysical Research (Space Physics)*, *118*, 3672–3691, doi:10.1002/jgra.50347.

Sonnerup, B. U. O. (1980), Theory of the low-latitude boundary layer, *J. Geophys. Res.*, *85*, 2017–2026, doi:10.1029/JA085iA05p02017.

Vaisberg, O. L., V. N. Smirnov, L. A. Avanov, J. H. Waite, J. L. Burch, D. L. Gallagher, and N. L. Borodkova (2001), Different types of low-latitude boundary layer as observed by interball tail probe, *Journal of Geophysical Research: Space Physics*, *106*(A7), 13,067–13,090, doi:10.1029/2000JA000154.

Wang, H., H. Lühr, and S. Y. Ma (2005), Solar zenith angle and merging electric field control of field-aligned currents: A statistical study of the Southern Hemisphere, *Journal of Geophysical Research (Space Physics)*, *110*, A03306, doi:10.1029/2004JA010530.

Wing, S., S.-i. Ohtani, P. T. Newell, T. Higuchi, G. Ueno, and J. M. Weygand (2010), Dayside field-aligned current source regions, *J. Geophys. Res.*, *115*, A12215, doi:10.1029/2010JA015837.

Wing, S., S.-i. Ohtani, J. R. Johnson, M. Echim, P. T. Newell, T. Higuchi, G. Ueno, and G. R. Wilson (2011), Solar wind driving of dayside field-aligned currents, *J. Geophys. Res.*, *116*, A08208, doi:10.1029/2011JA016579.

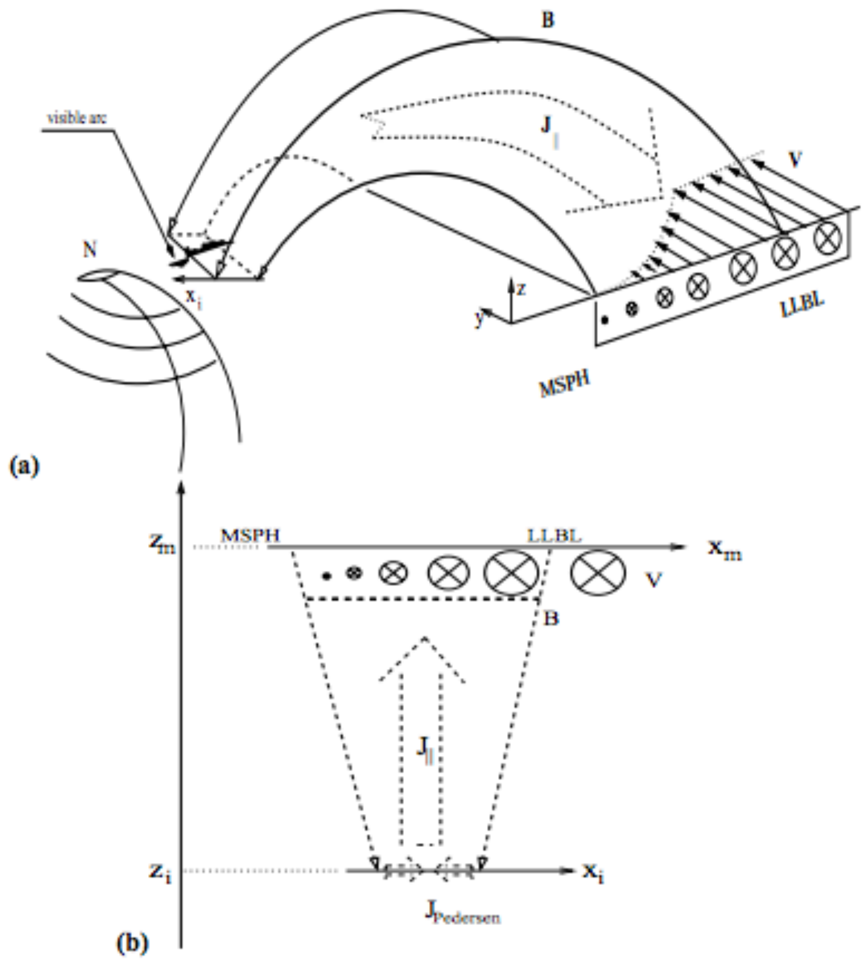

Figure 1. Diagram illustrating the geometry considered to study the coupling between a sheared flow LLBL and the ionosphere. (a) A schematic 3D view of the magnetosphere flank; (b) a simpler, conical geometry adopted to describe a flux tube extended from ionospheric altitudes (z_i) to the magnetosphere (z_m). The velocity profile is illustrated by circles with radius proportional to the local value of the shear velocity (adapted from *Echim et al.* [2007].

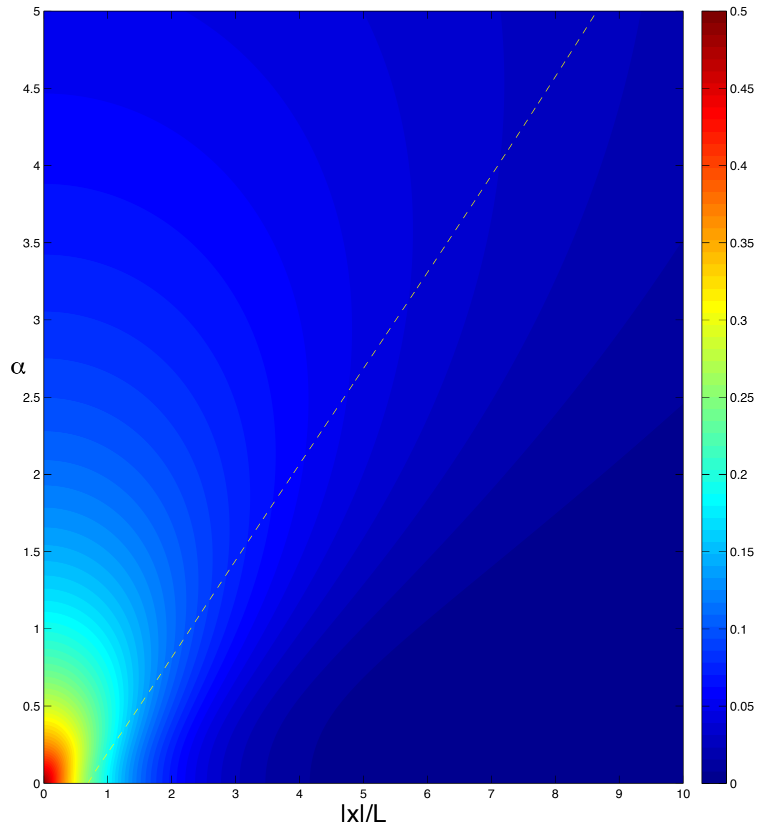

Figure 2. Parallel current, normalized to $\kappa V_0 B_0 \sqrt{b} L$, as a function of $|x_i|/L$ and α. The dotted line indicates the a value $|x|/L$ where $j_\parallel = j_{\parallel,\max}/2$.

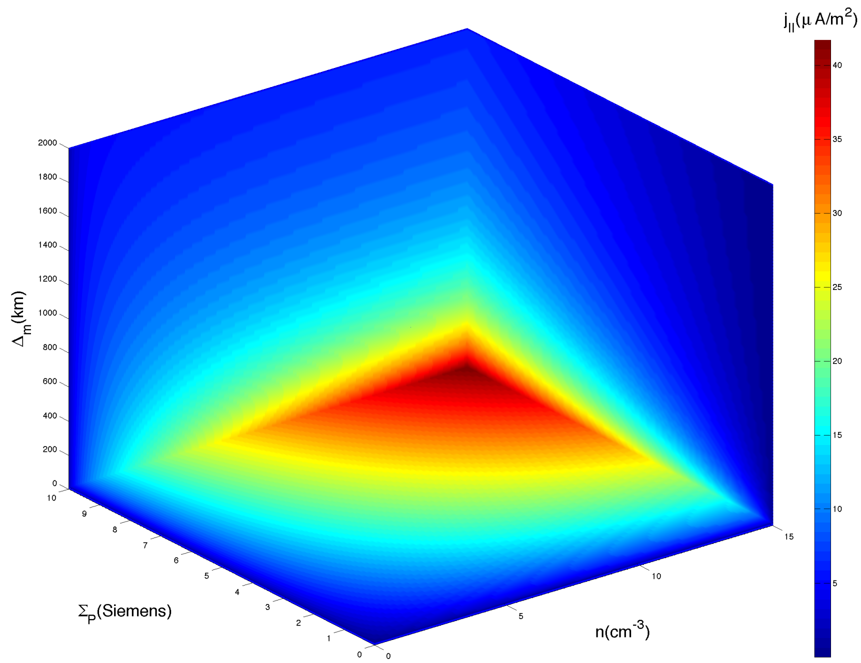

Figure 3. Maximum parallel current (Equation 17) as a function of boundary layer density, ionospheric conductivity, and velocity shear layer thickness with $V_0 = 200$km/s and $B_0 = 50$nT.

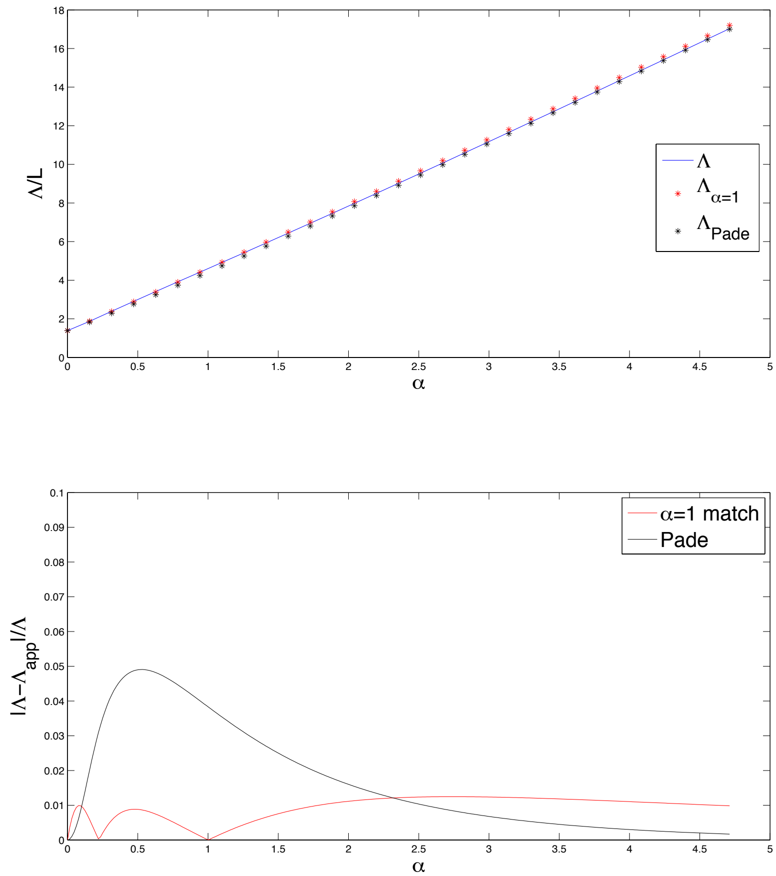

Figure 4. The upper panel shows the full width at half maximum, Λ, obtained from Equation 15, while the points displayed show the approximate values using the Padé approximation and the fit at $\alpha = 0$. The lower panel shows the relative error from using such a solution. The advantage of the uniform solution is that the error is distributed evenly and is roughly bounded by 1% compared to 5% for the Padé approximation.

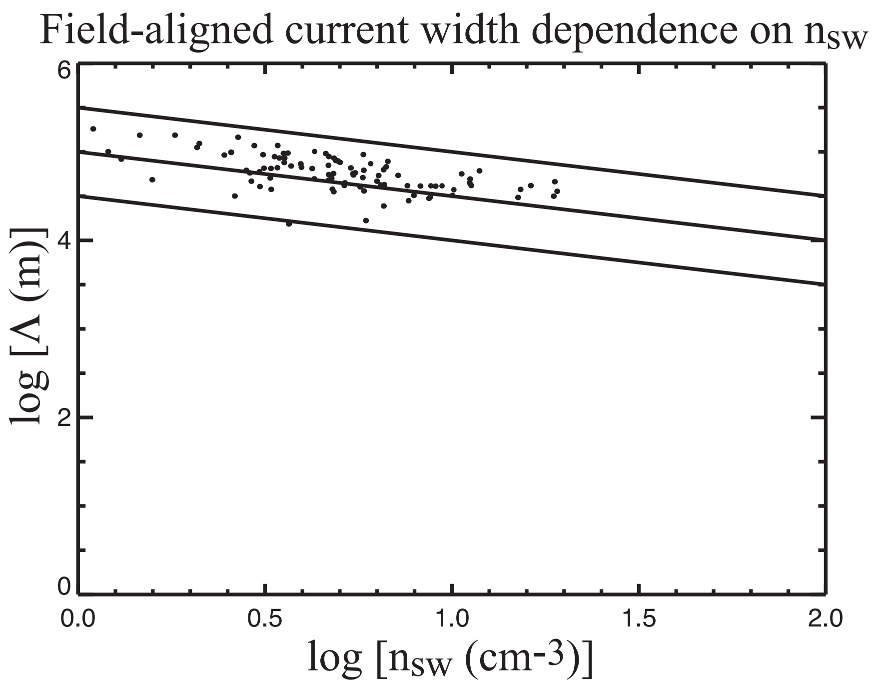

Figure 5. Field-aligned current width (Λ) decreases with increasing n_{sw} for small α. The solid black lines have slope = -0.5, which is the expected slope from Equation 35 for small α.

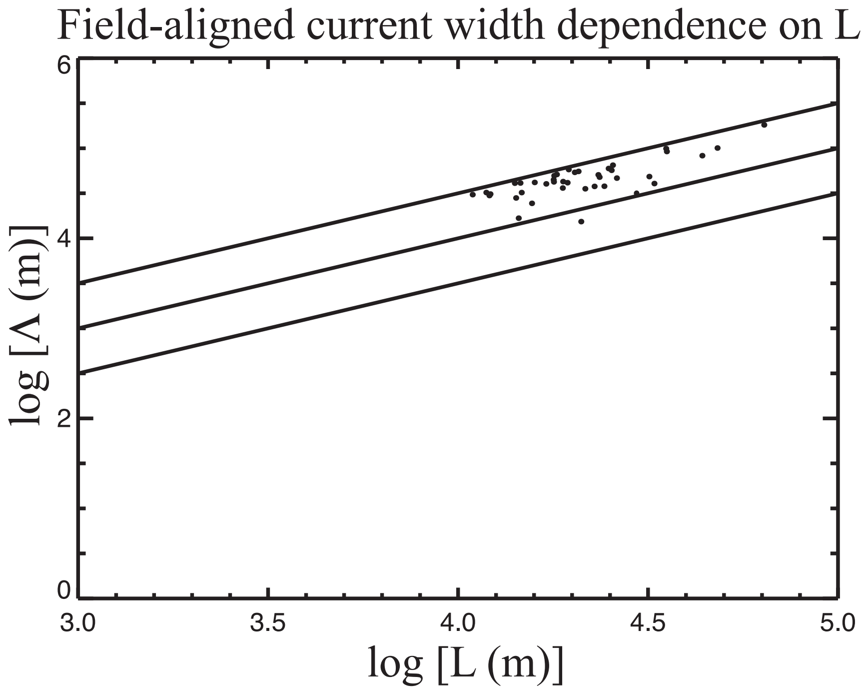

Figure 6. Field-aligned current width (Λ) as a function of L for small α. The solid black lines have a slope = 1, which is the expected slope from Equation 35.

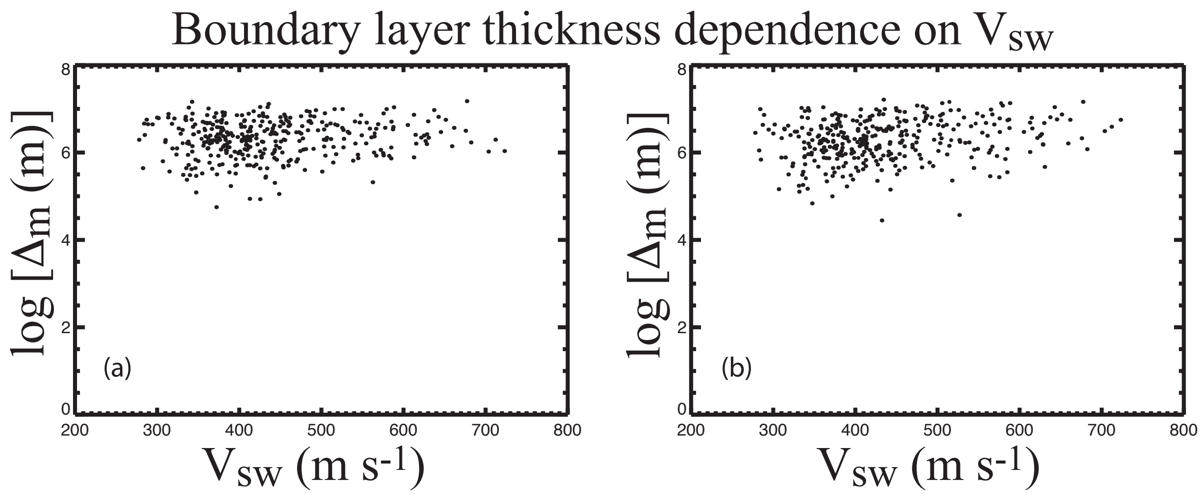

Figure 7. The magnetospheric boundary layer (Δ_m) has a weak dependence on V_{sw}. Δ_m is calculated using two methods: (a) from Equation 42 and $\Delta_m/\Delta_i \sim \sqrt{B_m/B_i}$ and (b) from Equation 23. Both methods return $\Delta_m s$ that are consistent with each other. The scatter is larger in (b) than in (a) partly due to the larger number of free parameters and the uncertainties in estimating those parameters in Equation 23 than in Equation 42.

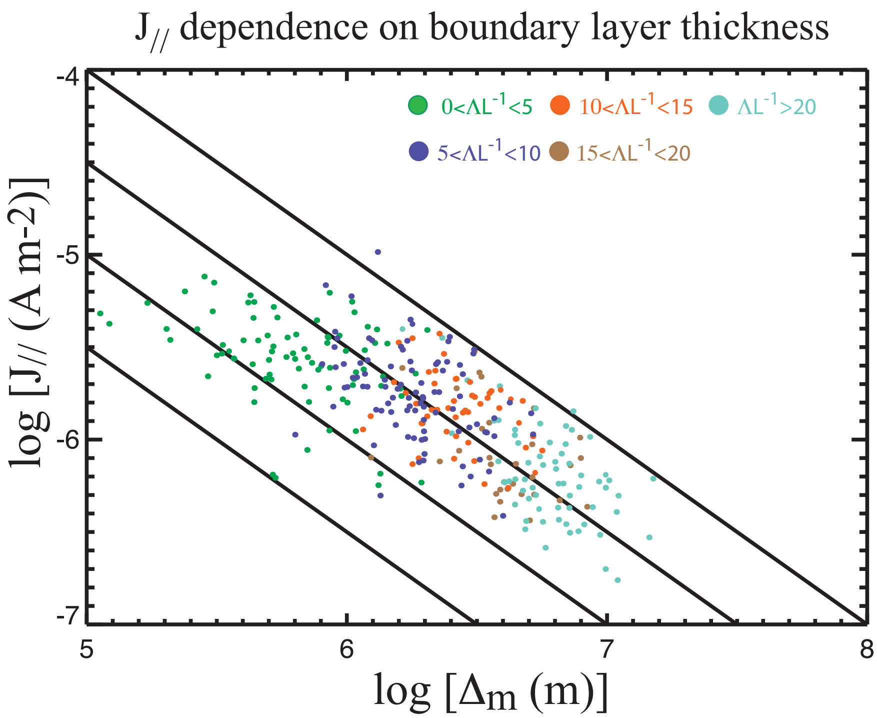

Figure 8. Field-aligned current density ($J_{//}$) decreases with increasing Δ_m. The large scatter can be attributed partly to the large number of free parameters relating the two parameters as expressed in Equation 23. The solid lines have slope = -1, which is expected from Equation 23. The lines do not fit green dots ($\Lambda/L < 5$) as well because for small α, $J_{\|}$ should be independent of Δ_m, as indicated by Equation 19.

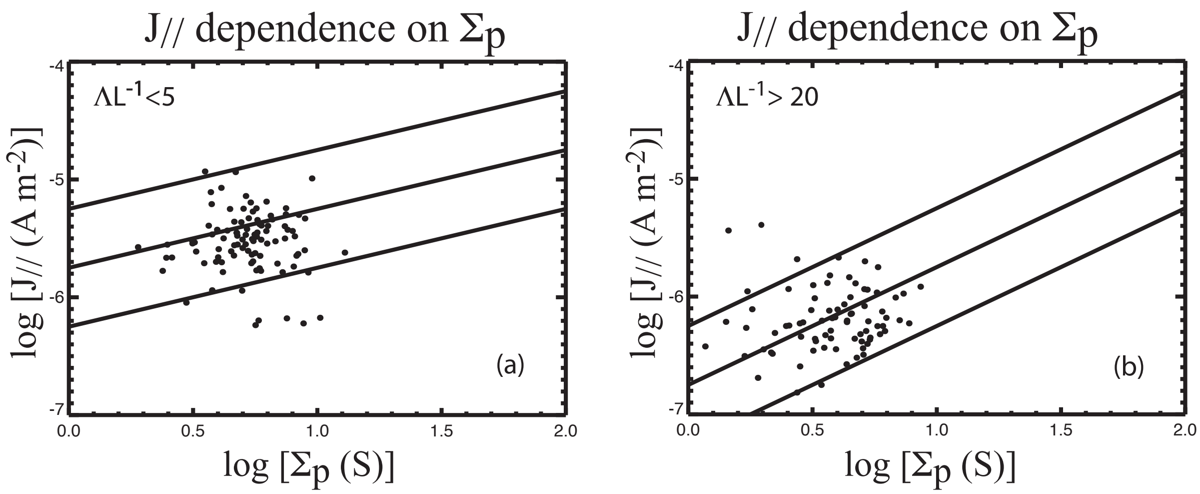

Figure 9. Field-aligned current density ($J_\parallel$) increases with Σ_p, but there is a dependence on α. (a) for $\Lambda/L < 20$ (large α), the points tend to align with lines of slope = 0.5 , which is consistent with Equations 19 and 23 while (b) for $\Lambda/L > 20$ (large α), the points tend to align with lines of slope = 1, which is consistent with Equation 21. The large scatter can be attributed partly to the large number of free parameters relating the two parameters as expressed in Equation 23.

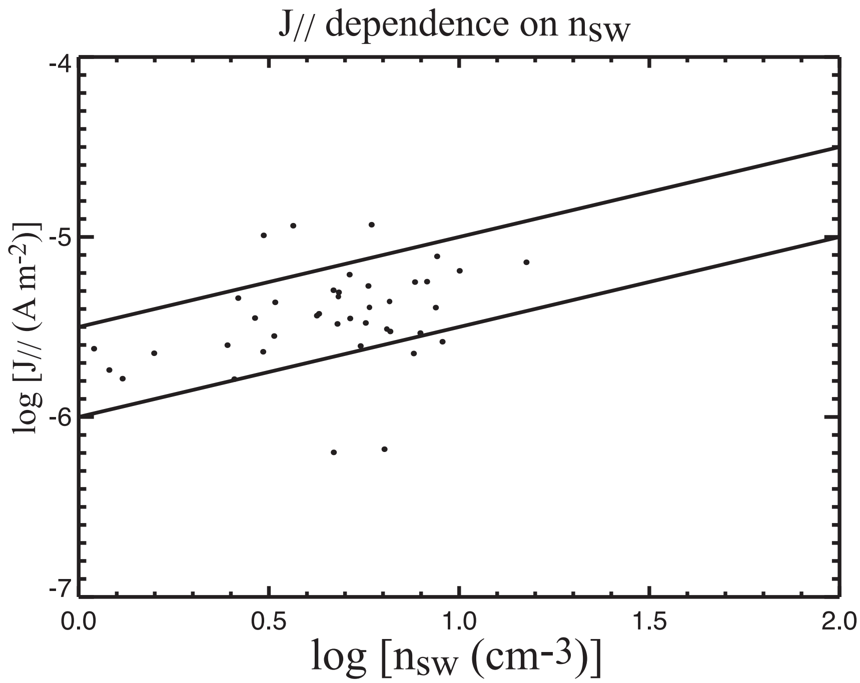

Figure 10. Field-aligned current density ($J_{\|}$) increases with n_{sw} for small α ($\Lambda/L < 3$). The solid black lines have slope = 0.5, which is expected from Equations 19 or 23.

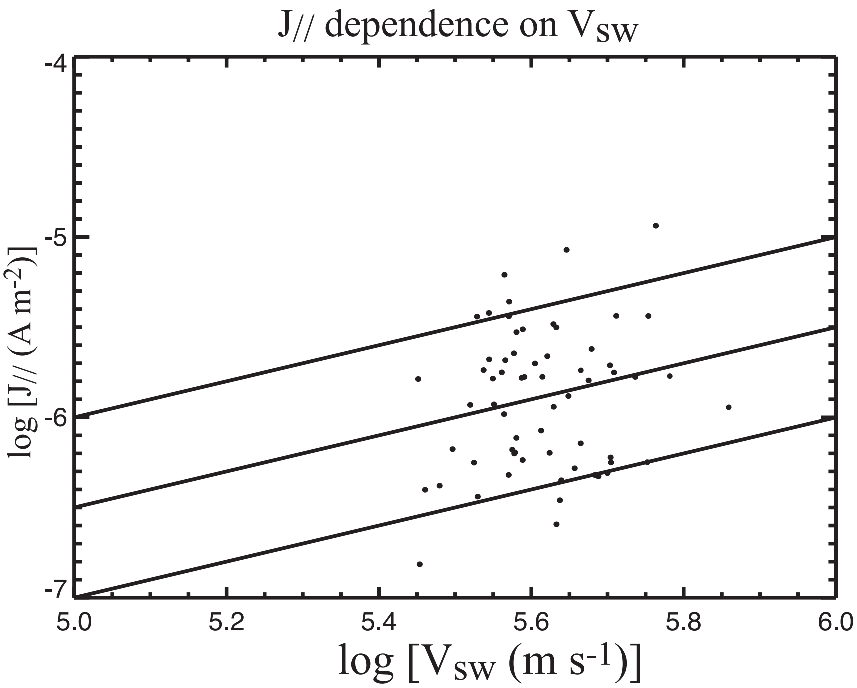

Figure 11. Field-aligned current density ($J_{\|}$) increases with V_{sw}. The solid black lines have slope = 1, which is expected from Equation 23.

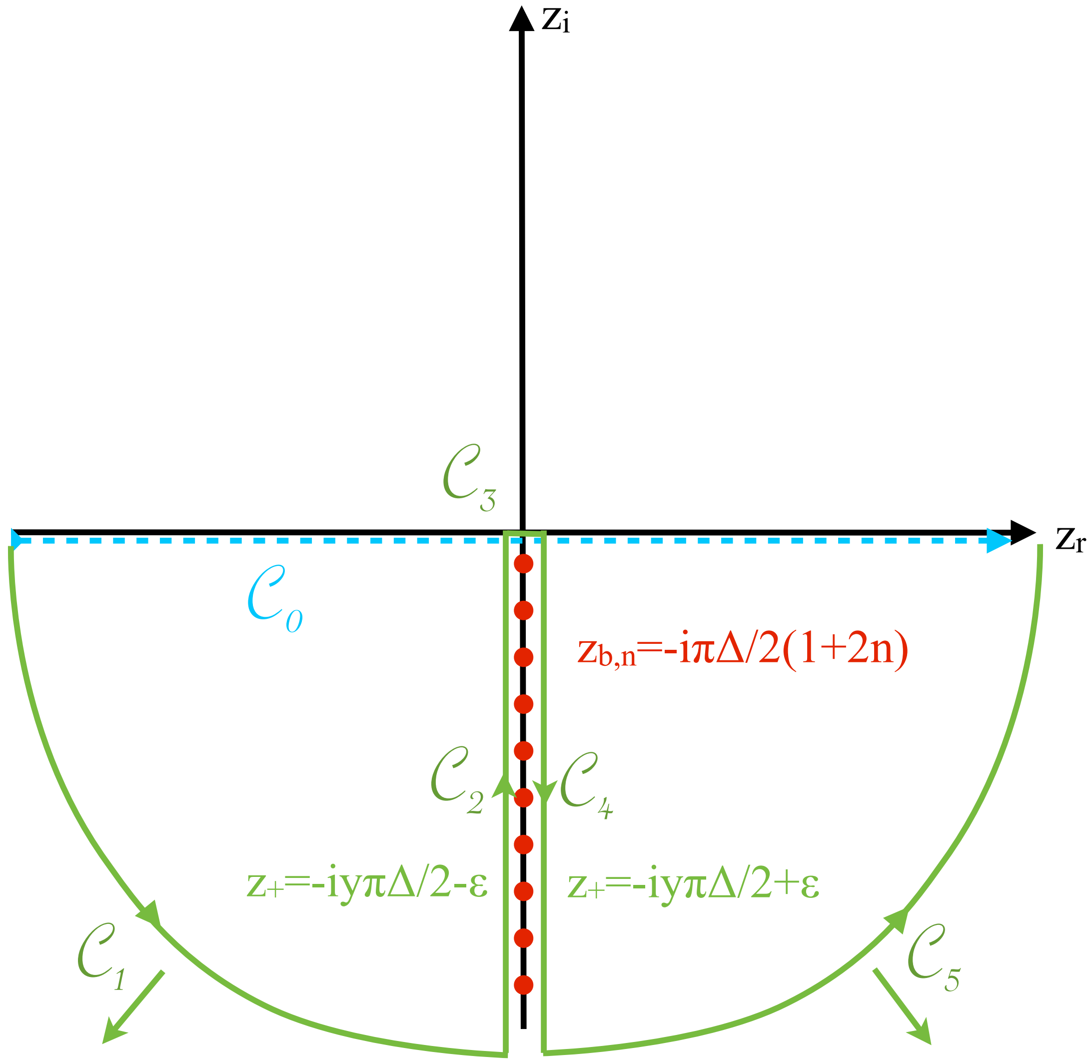

Figure 12. The Fourier transform of $\Delta_i \log(2\cosh(x/\Delta_i))$ is obtained by deforming the path of integration as shown in the complex plane. The original path, $\mathcal{C}_0$ runs along the real axis (just below the real axis $\Re(q) > 0$ to ensure convergence). This path is deformed into a new path in the complex plane with five segments as shown. The integrals along paths $\mathcal{C}_1$ and $\mathcal{C}_5$ vanish in the limit that the radius of the path becomes large. The small segment, $\mathcal{C}_3$, of the path along the real axis vanishes in the limit of small ϵ. The only non-vanishing contributions come from paths $\mathcal{C}_2$ and $\mathcal{C}_4$, which do not cancel because of difference in the argument of the logarithm function resulting from the branch cuts at $z_{b,n} = -i\pi\Delta_i/2(1+2n)$ where n is an integer.

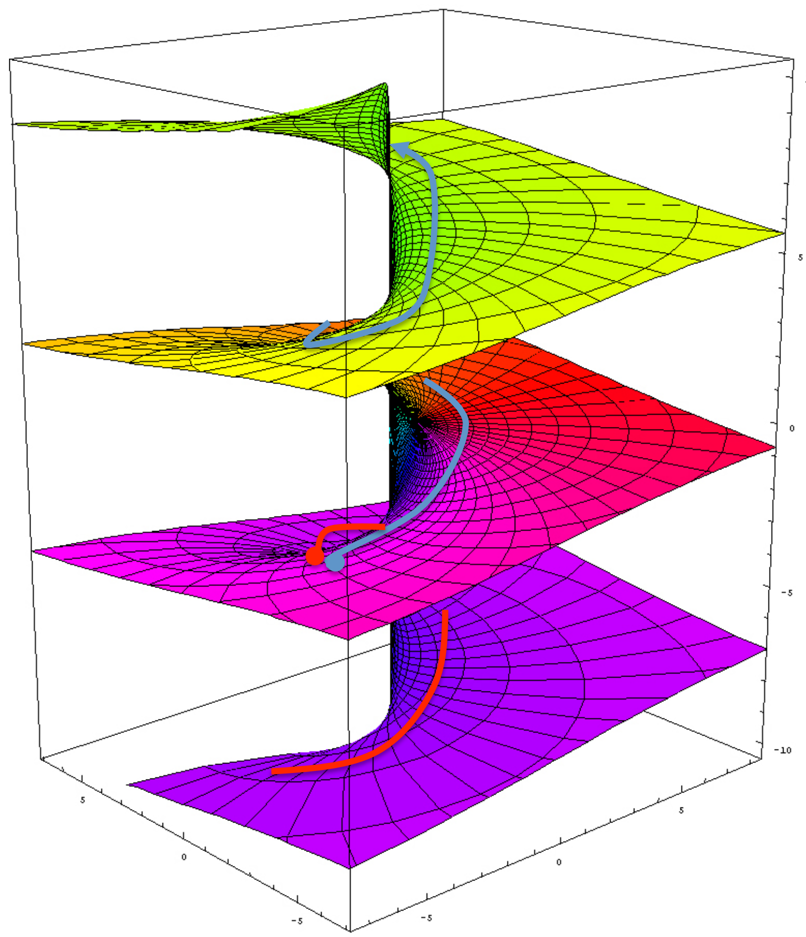

Figure 13. The argument of the logarithm moves across branches as each branch point is passed. Because cosh is an even function of real argument along the real axis, the argument of both paths is chosen to be zero as the real axis is approached. As y increases from 0, the path that has $\Re x < 0$ (depicted in blue) has increasing argument, while the path with $\Re x < 0$ has decreasing argument. The difference in argument along the paths is 0 from $y = 0$ to $y = 1$, 2π from $y = 2$ to $y = 3$ and so forth.

Princeton Plasma Physics Laboratory
Office of Reports and Publications

Managed by
Princeton University

under contract with the
U.S. Department of Energy
(DE-AC02-09CH11466)

P.O. Box 451, Princeton, NJ 08543
Phone: 609-243-2245
Fax: 609-243-2751

E-mail: publications@pppl.gov

Website: http://www.pppl.gov